

Rheological, microstructural characterization and interlayer bonding of 3D printed cement mortars with slump-retaining polycarboxylate superplasticizer

Tinghong Pan^{a, b}, Yaqing Jiang^{a*}, Xuping Ji^{a, c*}

^a College of Mechanics and Materials, Hohai University, Nanjing 211100, China;

^b Yunnan Provincial Key Laboratory of Civil Engineering Disaster Prevention,

Faculty of Civil Engineering and Mechanics, Kunming University of Science and

Technology, Jingming South Road, Kunming, 650500, China;

^c State Key Laboratory of High Performance Civil Engineering Materials, Jiangsu

Sobute New Materials Co. Ltd., Nanjing, 211103, China;

*corresponding author

E-mail addresses: yqjiang@hhu.edu.cn (Y. Jiang), xpji@hhu.edu.cn (X. Ji).

Abstract:

For the 3D printing cementitious materials (3DPC), high rate of structural build-up is recommended to ensure the buildability and stability of printed structures, while it results in a rapidly loss of workability and plasticity and thus lead to a challenge for the interlayer bonding. This paper mainly studies the possibility of improving the interlayer bonding of 3D printed structures by adjusting the change law of rheological properties with time under the premise of buildability. Results indicate that although the initial fluidity of slump-retaining polycarboxylate superplasticizer

* Corresponding authors.

E-mail addresses: yqjiang@hhu.edu.cn (T. Pan), xpji@hhu.edu.cn (X. Ji).

(TSRS) is slightly lower than that of high dispersion polycarboxylate superplasticizer (DPCS), its loss of fluidity with time is lower. Long duration of fluid properties promotes permeate and fusion between adjacent layers, resulting in lower plane porosity and lower fractal dimensions of pore structures at the interlayer zone. The average plane porosity and maximum plane porosity at the interlayer zone are linearly related to the interlayer bond strength. Therefore, long duration of fluid properties also results in high interlayer bond strength. For 3DPC, adjusting the change law of rheological properties with time is important as adjusting the initial rheological properties, both of them are critical parameters that affect the printability and interlayer bond strength.

Keywords: Cementitious materials; 3D printing technology; Rheological properties; Interlayer bond strength, X-ray micro computed tomography

1. Introduction

Intelligent construction is an important development direction of the construction industry in the future. The 3D printing cementitious materials(3DPC) is the core and key to realize intelligent building manufacturing [1–3]. For the construction industry, 3DPC technology breaks through the limitations of the traditional formwork–casting method, and may build structures with complex shapes that cannot be built by the traditional formwork–casting method. Compared with traditional formwork–casting method, 3DPC technology bring significant technological advancements for building–construction industry, such as no needs for formwork [4, 5], reducing design time and execution period reducing labour costs [2, 6, 7], reducing wastes and increasing freeform architectural designs [6, 8].

In the 3D printing process, printable cement–based ink is extruded through the printing nozzle via the pumping force of concrete pump or the mechanical extrusion force of printhead [9, 10]. Through the movement of nozzle along a predetermined path, the printing ink is deposited layer–by–layer to form the final 3D structure. After the printing ink out of nozzle, it will transit from fluid state to quasi–solid or solid state quickly and rapidly lose fluidity and plasticity, due to the structural build–up

process and cement hydration process [11, 12]. This has a positive effect on the buildability and stability of 3D printed structures, due to the rapid transition of printing ink from fluid to quasi-solid or solid leads to required strength to sustain its self-weight initially and the weight of the subsequently printed layers on top of it [13, 14]. However, this has a negative effect on the interlayer bonding of 3D printed structures [15–17].

In case of both “contacting” layers being in a fluid state or one being in a fluid state and another quasi-solid state, the common case in extrusion-based 3D printing, the rheological properties [18] of both “substrate” and “overlay” layer, significantly influence the interlayer bonding. For “substrate” layer, losing of fluidity and plasticity and forming a quasi-solid or solid structure may result in a fusion challenge between the “overlay” layer and the “substrate” layer, especially under the condition of lack of vibration [19, 20]. Furthermore, with ageing consolidation process, the evaporation and drying of water on the surface of “substrate” layer would result in insufficient hydration and high porosity. This negatively affects the interlayer bonding of 3D printed structures. For “overlay” layer, good wettability and spreading is expected to successfully fill and permeate into the pores and cracks in the surface of initial layer, thus resulting in an initial formation of mechanical interlock between the two zones [21–23]. If the newly deposited layer has a lower workability or rapidly loses its fluidity and plasticity, it can't penetrate into the roughness profile, therefore exhibits not only poor anchorage but reduced contact area [22, 24, 25]. Taylor et. al. reported that using a paste layer with higher and sustained flow characteristics increases the bond strength of between adjacent layers [24]. Vibration may be used to increase the flowability of cement-based materials and to enable physical intermixing of layers. However, external vibration is risky for the already deposited layers, since it would disrupt the buildability [19, 20, 26].

Except the rheological properties of both “substrate” and “overlay” layer, the physical and chemical states difference between two layers also significantly affects the interlayer bonding of 3D printed structures [26]. The printing time interval is the main driver of this difference. For a short-time interval, there is no significant

difference between the states of “substrate” and “overlay” layer. Extending the time interval will increase the difference between the states of “substrate” and “overlay” layer, such as modulus/stiffness difference, rheological properties difference and surface state (surface moisture) difference, due to the time-dependent physical and chemical states of cement-based materials [27–29]. Continuously extending the time interval, the adhesion between adjacent printing layers can even be regarded as the bond between old and new concrete (this case will not occur in 3D printing process).

In micro-scales, all the above consequences may attribute to the microstructure of the printed structures, particularly the void fractions, interconnectivity and space distribution within the interlayer zone of printed structures. For the quasi-brittle 3D printed structures, extending the porosity within the interlayer zone is the possible reason for the lower interlayer bond strength between adjacent printed layers [30, 31]. Air-void systems within interlayer zone act as the stress concentration sites and also promote the crack propagation under loading, which may decrease the fracture energy and the interlayer bond strength of printed structures. Panda et al. [30] and Tay et al. [32] found that macropores or air-void systems interlayer bond strength may be due to the lack of fusion, which significantly decrease the interlayer bond strength between two layers. Furthermore, the air-void systems between two layers provide channels for the faster ion ingress, which may facilitate corrosion of reinforcing steel in 3D printed structures via carbonation or chloride ingress [33]. Therefore, it is necessary to reduce the air-void systems and increase the contact area between adjacent printed layers to improve the interlayer bond strength. The rheological properties of both “substrate” and “overlay” layer, printing time interval, microstructure and interlayer bonding properties of printed structures are interrelated. Therefore, the correlation between them should be further studied.

In order to explore the correlation of interface characteristics between 3D printing layers, two different types of polycarboxylate superplasticizers (a high dispersion polycarboxylate superplasticizer DPCS and a slump-retaining polycarboxylate superplasticizer TSRS) were used to control the time-dependent rheological properties, and the physical and chemical state differences between

adjacent layers were adjusted through different printing time intervals (20 s, 30 min and 60 min). The rheological properties of 3D printed cement mortars with different types of polycarboxylate superplasticizer were characterized via BROOKFIELD RST-SST rheometer, the microstructure of 3D printed structure was measured by X-ray CT computed tomography system, and the interlayer bond strength of 3D printed structure was measured by direct tensile test.

2. Materials & methods

2.1 Printable mixture design

Two printable mixtures that were developed by the authors [34] were used in the current study, As shown in Table 1. Ordinary Portland cement (OPC, Type II, 42.5 grade, Nanjing Conch Cement Co. Ltd) was selected as the binder. Attapulgite clay (Jiangsu Jiuchuan Nano-material Technology Co.Ltd.) exfoliated into nanoparticles (called as nano clay, Nc) shaped with 135 nm average length and about 58 nm diameter was selected as the thixotropic admixture [35, 36]. Hydroxy propyl methyl cellulose (HPMC, Renqiu Cheng Yi Chemical Co.Ltd.) was selected as viscosity modifier. The chemical compositions of OPC and Nc were given in Table 2. Except for the type of superplasticizer, both mixture compositions were kept identical, for instance, binder to sand ratio of 1:1.5, water to binder ratio of 0.32, the dosage of Nc, HPMC and superplasticizer were fixed as 0.8 wt%, 0.24 wt% and 0.3 wt% (of the binder mass), respectively. Two types of superplasticizers: a high dispersion polycarboxylate superplasticizer (DPCS), and a slump-retaining polycarboxylate superplasticizer (TSRS) were employed.

The Fourier transformer infrared spectra (FTIR), Gel permeation chromatography (GPC) and TOC adsorption of DPCS polymer and TSRS polymer were reported in Appendix A, Appendix B and Appendix C.

Table 1. Proportion of 3D printing cement mortars.

Material	Cement	Quartz sand	Water	Nano-clay	HPMC	TSRS or DPCS polymer
Quantity(g)	1400	2100	460	11.2	3.5	4.2

Table 2. Chemical compositions of OPC (Type II) and Nc [wt.%].

Materials	CaO	SiO ₂	Al ₂ O ₃	FeO ₃	Na ₂ O	MgO	K ₂ O	SO ₃	TiO ₂	L.O.I
OPC	62.60	21.65	5.56	4.32	0.24	0.84	0.76	2.85	—	1.27
Nc	9.62	58.4	26.73	0.51	0.21	0.20	3.05	—	0.15	1.13

2.2 Specimen preparation

JJ-5 planetary cement mortar mixer was used to mixing materials. Firstly, dry batch, such as cement, fine aggregate and nano clay were mechanically mixed for one minute in the cement mortar mixer to form a homogenous mixture. Next, the water and superplasticizer were poured into the mixer and mechanically mixed with dry batch for 60 s at a slow speed. Then stopping for 30 s to scrape off the residual slurry on the wall of the mixer. Lastly, the cement paste was quickly mixed for 90 s. The whole mixing process lasted for 3 minutes, since water was mixed with dry batch. The mixture was immediately placed into a specific container for rheological properties test and poured into 3D printer.

2.3 Rheological Measurements

Rheological behavior is one of the most important performance, in the study of 3D printing ink, which play a significant role in describing the pumpability, extrudability and buildability of mixtures [37, 38]. In this work, the rheological properties of mixtures, such as viscosity, yield stress, static yield stress and the area of thixotropic hysteresis loop are characterized using BROOKFIELD RST-SST rheometer. Two rheological testing protocols are proposed to quantitatively measure the area of thixotropic hysteresis loop and static yield stress, respectively.

2.3.1 Thixotropic hysteresis loop

Thixotropic hysteresis loop method is one of the most popular method to evaluate the thixotropy of cement mortar [39], as shown in Fig. 1. The mixtures are first pre-sheared for 120 s by applying a shear rate sweep from 0 1/s to 100 1/s, which is mainly used to create a uniform environment with little test error. Then, after 10 s of rest, an increasing shear rate ramp from 0 1/s to 100 1/s within 100 s is applied to produce the up-curve of the flow test. Finally, the shear rate decreases from 100 1/s

to 0 1/s within 100 s to obtain the down-curve of the flow test. The up-curve and down-curve of the flow test form the envelope region of hysteresis loop, as shown in Fig. 1(b). The area of thixotropic hysteresis loop is related to the energy needed to destroy the flocculation structure, which can be expressed by Equation (1).

$$A = \int_{\dot{\gamma}_{min}}^{\dot{\gamma}_{max}} \tau_1 \dot{\gamma} d\dot{\gamma} - \int_{\dot{\gamma}_{min}}^{\dot{\gamma}_{max}} \tau_2 \dot{\gamma} d\dot{\gamma} \quad (1)$$

where, A is the area of thixotropic hysteresis loop, $\dot{\gamma}$ the shear rate (1/s), τ_1 and τ_2 the maximum and minimum value of the shear stress, respectively.

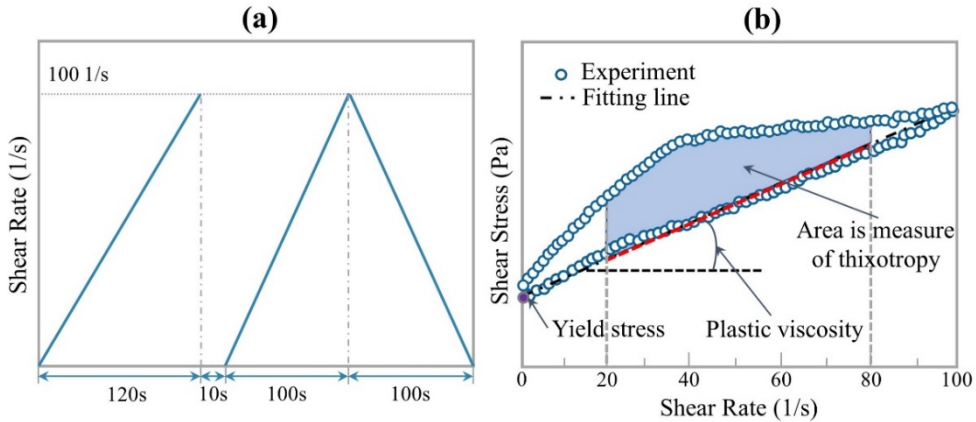


Fig. 1. Rheological testing protocols for thixotropic hysteresis loop.

2.3.2 Static yield stress

This protocol is used to monitor the development of static yield stress with resting time. After mixing, mixture was divided into 10 groups to measure the value of static yield stress at different resting time. 10 groups of samples are put into different glass bottles, and then each group is manually stirred for 1 minute to ensure that all samples have the same initial structure. After resting for a certain time (0 s, 150 s, 300 s, 450 s, 600 s, 750 s, 900 s, 1050 s, 2000 s and 3000 s, respectively), the sample is taken out to test the static yield stress, as shown in Fig. 2(a). In the static yield stress test protocol, a constant shear rate of 0.02 1/s is used. The maximum shear stress on the shear stress vs time curve is defined as static yield stress [40], as shown in Fig. 2(b). According to the research results of Ivanova and Yuan et al. [41, 42], the

development of static yield stress can be used to monitor the structural build-up of cement-based materials.

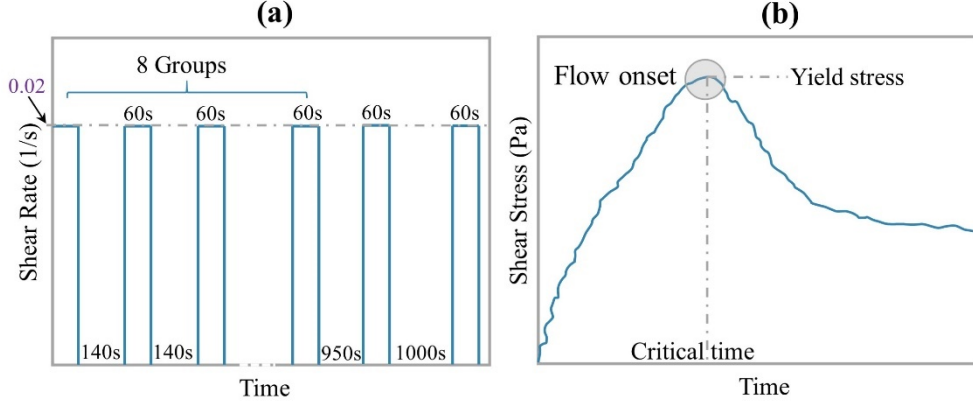


Fig. 2. Test protocols of static yield stress (a), and static yield stress obtained from the peak value (b).

2.4 Printing device and printing parameters

A self-made laboratory level gantry 3D printer with forming space of 500 mm × 500 mm × 500 mm is used with a screw extrusion, as shown in Fig. 3. A square nozzle with opening of 40 mm × 20 mm is used in this work, which results in a large surface contact area between the adjacent extruded layers. The moving speed v of nozzle is set as 60 mm/s and the height h between the nozzle and the build surface is fixed at 25 mm. The screw rod driven by stepper motor is used to extrude the 3D printed ink out of a nozzle and the extrusion rate E is set as 12 mL/s, by adjusting the rotation rate of screw rod.

Double-layer structures with different types of superplasticizers and different printing time interval are prepared for the interlayer bonding strength test and X-CT test, as shown in Table 3. The actual printed results are reported in Fig. 4. After double-layer structure is printed, the strip sample is cut into small squares with a length of 40 mm, immediately. Then the cut specimen is cured in the standard curing environment for 28 days.

Table 3. Sample with different types of superplasticizers and different printing time interval.

No.	Printing time interval (s)	Types of superplasticizers
DPCS/T20	20	DPCS
DPCS/T1800	1800	DPCS
DPCS/T3600	3600	DPCS
TSRS/T20	20	TSRS
TSRS/T1800	1800	TSRS
TSRS/T3600	3600	TSRS

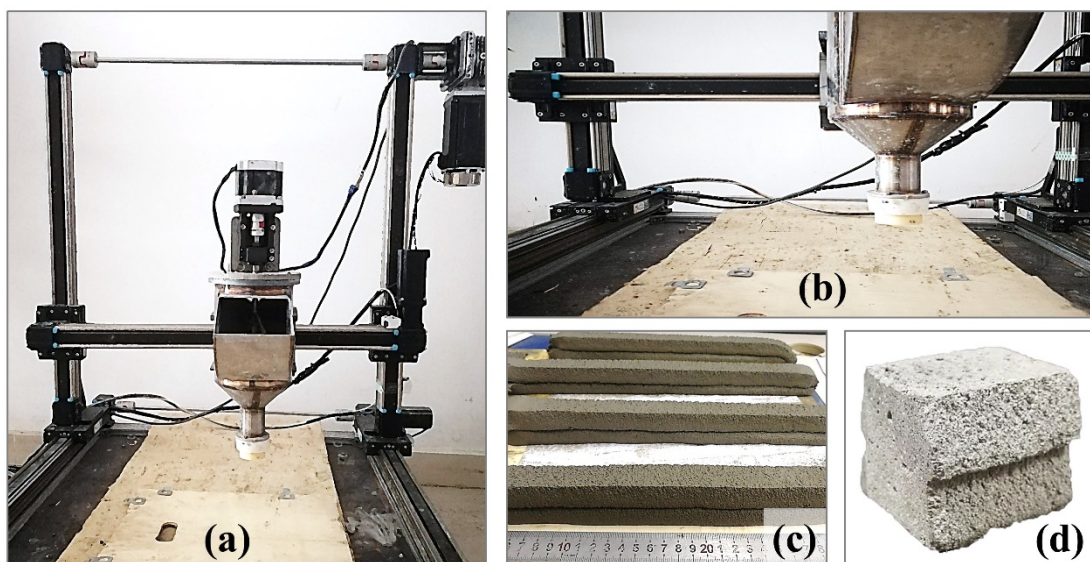


Fig. 3. 3D Printing device (a), printing nozzle (b), double-layer structures without cutting (c) and with cutting (d).

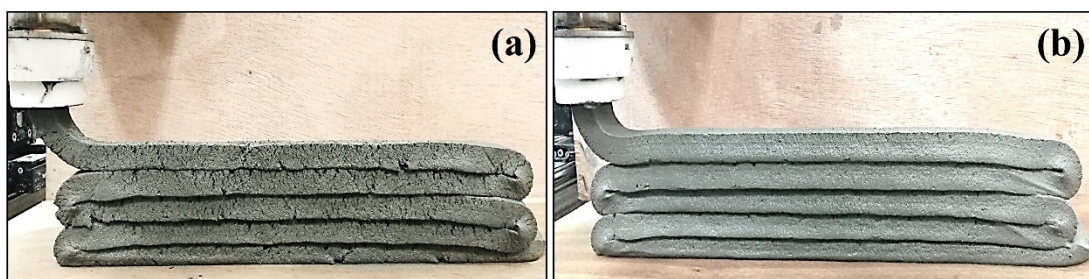


Fig. 4. Demonstration of 3D printability of mixtures: (a) DPCS/T20, (b) TSRS/T20.

2.5 X-ray computed tomography

2.5.1 X-CT image acquisition and segmentation

Microstructure of printed structures are performed using a Nikon metrology X-ray CT computed tomography (Nikon XTH) system supplied from Nikon metrology instruments.

2.5.2 Air void characterization

In this work, the plane porosity and fractal dimension of 2D slice that perpendicular to the stacking direction of the printed layer are used to quantitatively characterize the pore characteristics within the interlayer zone of 3D printed cement mortars. Porosity can directly reflect the compactness of the printed structures, and can be obtained from the proportion of pore area in the total area of 2D slice.

$$\phi = \frac{A_V}{A_T} \quad (2)$$

where ϕ is the plane porosity, A_V the area of void space in 2D slice, A_T the total area of 2D slice.

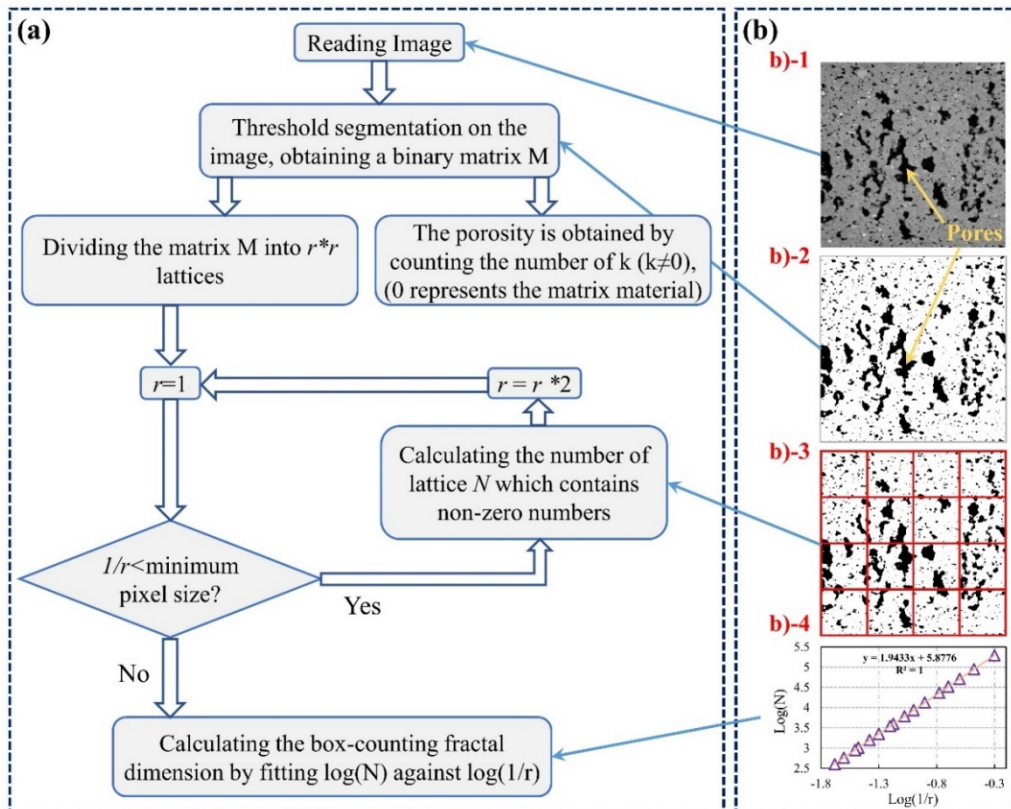


Fig. 5. The process of solving the plane porosity and box-counting dimension of 2D slice

Fractal dimension can characterize the complexity of structure from a multi-scale perspective [43]. Mandelbrot et. al. [44] has pointed out that fractal dimension provides a new approach to describe the self-similarity and complexity of objects. Many calculation methods, such as box-counting dimension, triangulation and power spectrum, have been used to characterize the fractal characteristics of structures [45]. In this work, box-counting dimension is used to evaluate the fractal characteristics of pores in 2D slices. For complex structures with autocorrelation, the box-counting dimension D^b can be expressed as:

$$D^b = \log(N^k)/\log(1/k) \quad (3)$$

where N^k is the minimum number of grids that overlaying the surface of complex structure with square grid with side length k . Box-counting dimension indicates that the number of square grids N^k increases with the decrease of side length k , and the calculation algorithm of box-counting dimension on 2D slice is shown in Fig. 5.

2.6 Interlayer bonding strength

Before the tensile loading test, the upper and lower ends of the specimen have been cut and polished, and the total thickness of the specimen after polishing is about 20 mm. Then, the samples are bonded to the molds with high-strength epoxy glue, as shown in Fig. 6. In the tensile bond strength testing, tensile loading at a loading speed of 0.035 ± 0.015 MPa/s is applied to both the upper and lower ends of specimen. The tensile bond strength is calculated through the ratio of maximum tensile force to effective bonding area.

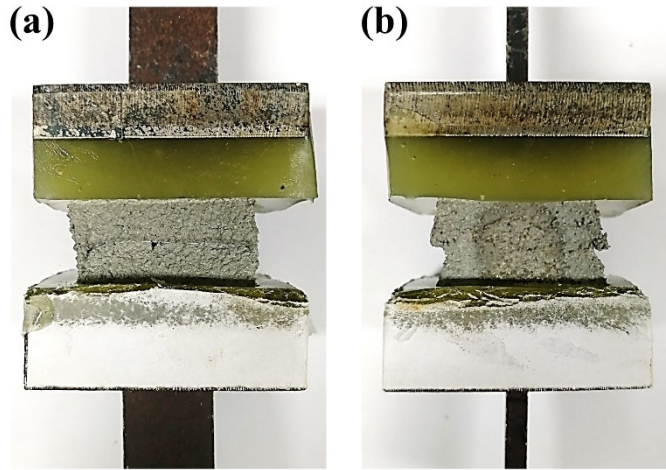


Fig. 6. Schematic of sample preparation for interlayer bond strength test.

3. Results

3.1 Rheological properties of cement mortars

The test results of thixotropic hysteresis loop, fluidity of mortar and static yield stress are shown in Fig. 7(a, b, d). In the up-curve of the thixotropic hysteresis loop testing protocols, there are more flocculation structures in the cement suspension, which increases the shear resistance of the rotor, and results in a higher shear stress [46]. In the down-curve of the thixotropic hysteresis loop testing protocols, part of the flocculation structure is destroyed, which decreases the shear resistance of the rotor and results in a lower shear stress than that in the up-curve [46]. The difference between the up-curve and down-curve is attributed to the content of flocculation structures in the cement suspension. Compared with DPCS polymer, TSRS polymer significantly increases the thixotropic hysteresis loop area of cement mortar, as shown in Fig. 7(a), which indicates that there are more (about twice) flocculation structures in the cement suspension with TSRS than that with DPCS.

Fig. 7(b) shows the initial fluidity of cement mortar with DPCS polymer is higher than that with TSRS polymer, which indicates that the DPCS polymer has better dispersion performance. However, the fluidity loss of cement mortar with DPCS polymer is higher than that with TSRS polymer, which indicates that the TSRS polymer has better slump-retention performance.

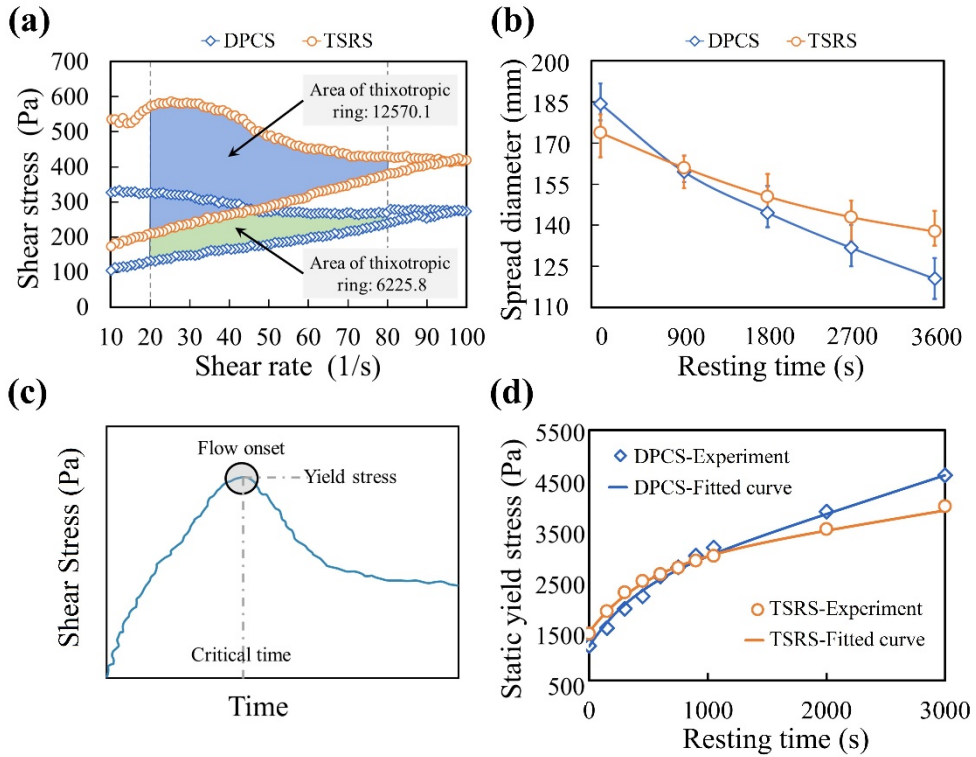


Fig. 7. The test results of thixotropic ring area (a), tripping table fluidity (b) and static yield stress (d) of cement mortar.

Fig. 7(d) reports the time-varying curve of static yield stress, which can be fitted by a nonlinear equation [34], and the fitted results are summarized in Table 4. The TSRS polymer improves the short-term structural build-up rate R_{thix} , but it significantly decreases the long-term structural build-up rate A_{thix} . This means that TSRS polymer promotes the physical flocculation. It is worth mentioning that the short-term structural build-up rate R_{thix} has same trend with the thixotropy represented by thixotropic hysteresis loop, which indicates that R_{thix} is a better indicator of appropriate thixotropic behaviour for cement mortars than A_{thix} . This is consistent with the research results of Kruger. et. al. [47].

Table 4. thixotropic parameters for cement mortar with DPCS polymer and TSRS polymer.

Types	τ_0 (Pa)	R_{thix} (Pa/s)	t_{perc} (s)	A_{thix} (Pa/s)
DPCS	1194	1.53	543.2	0.71
TSRS	1434	2.76	534.6	0.50

The difference of rheological properties between DPCS polymer and TSRS polymer may be attributed to the difference of their molecular structure and adsorption capacity, as reported in Appendix C. The adsorption capacity of cement to the DPCS polymer is higher than that of TSRS polymer at 10 min, which results in a significant steric hindrance effect, helps to destroy the flocculation structure. This may explain the higher flowability and smaller thixotropic hysteresis loop area of cement mixture with DPCS polymer at the initial stage [48, 49]. Then, with the cement hydration, the DPCS molecules adsorbed on the surface particles are continuously consumed, due to the deposition of hydration products (such as AFt and C-S-H, etc.) on the surface of cement particles, which decreases the number of PCs molecules in solution and decreases the adsorption capacity of cement to the DPCS polymer. This may be used to explain why the cement mortar with DPCS has higher fluidity loss and higher construction rate. Conversely, with the hydration of cement, more TSRS molecules would be released into the solution due to the hydrolysis of acrylamide in alkaline environment, which increases the number of PCs molecules in solution and increases the adsorption capacity of cement to the TSRS polymer. This explains why the fluidity-retention ability of the TSRS polymer is better than that of DPCS polymer.

3.2 Air–void systems within the interlayer zone

3.2.1 Air void content and distribution

The cement-based materials with different rheological properties may lead to various interlayer bonding behaviour at layer-to-layer interfaces, which would significantly affect the micro-structure of printed structures. In this work, plane porosity ϕ is used to characterize local air–void systems of 3D printed structures, the fractal dimension D^b is used to describe the complexity and irregularity of air–void systems [50]. Fig. 8 and Fig. 9 show how the plane porosity ϕ and the fractal dimension D^b change along the thickness of printed structures, respectively. These

values are obtained through digital image processing technology, as described in section 3.5.2 and the mean values and standard deviations are also calculated.

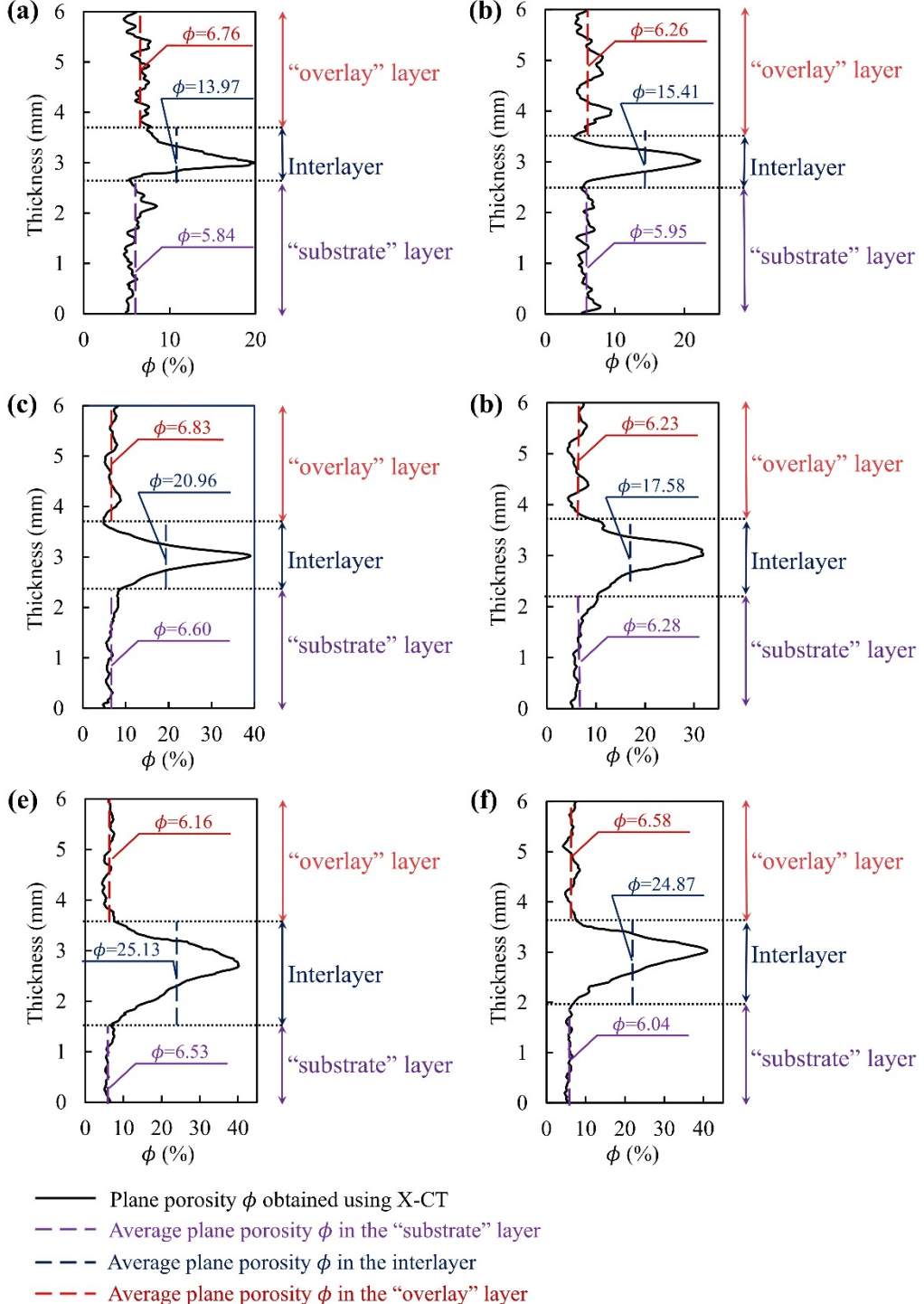


Fig. 8. The plane porosity ϕ as a function along the thickness of printed structures obtained on the basis of tests using the micro-CT method: (a) DPCS/T20, (b) TSRS/T20, (c) DPCS/T1800, (d) TSRS/T1800, (a) DPCS/T3600, (b) TSRS/T3600.

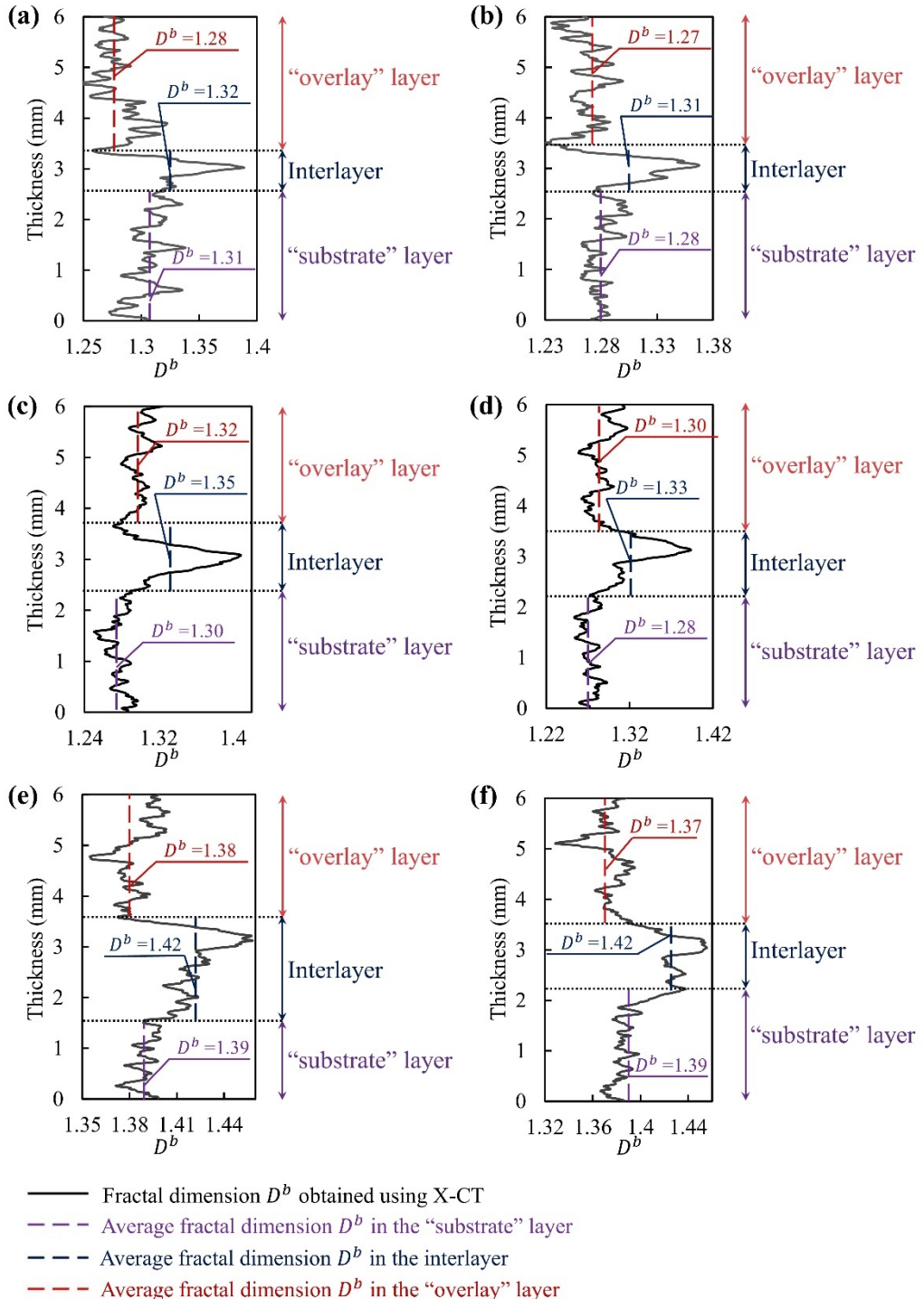


Fig. 9. The fractal dimension D^b as a function along the thickness of printed structures obtained on the basis of tests using the micro-CT method: (a) DPCS/T20, (b) TSRS/T20, (c) DPCS/T1800, (d) TSRS/T1800, (a) DPCS/T3600, (b) TSRS/T3600.

As shown in Fig. 8, the plane porosity in the middle-zone of the printed structures is higher than in other areas, which is due to the lack of fusion between the adjacent extruded layers. Based on the stabilization of the average plane porosity, where the interlayer zone begins and finishes is decided. Expending time interval may lead to a higher concentration of air–void systems in the interlayer zone, which would increase the average plane porosity in the interlayer zone and the thickness of the interlayer zone. For the samples with DPCS polymer, the average plane porosity ϕ in the interlayer zone with time interval of 30 min and 60 min were higher 50.1 % and 79.9 % than that with time interval of 20 s. For the samples with TSRS polymer, the average plane porosity ϕ in the interlayer zone with time interval of 30 min and 60 min were higher 14.1 % and 61.4 % than that with time interval of 20 s. Furthermore, extending time interval may also introduce the ‘wide’ macropores at the interlayer zone. Many ‘wide’ macropores concentrates in the interlayer zone may increase the complexity and irregularity of the air–void systems. For the samples with DPCS polymer, the average fractal dimension D^b in the interlayer zone with time interval of 30 min and 60 min were higher 2.3 % and 7.6 % than that with time interval of 20 s. For the samples with TSRS polymer, the average fractal dimension D^b in the interlayer zone with time interval of 30 min and 60 min were higher 1.5 % and 8.4 % than that with time interval of 20 s.

In addition, initial fluidity and loss of workability also significantly affects the microstructure of interlayer zone. The mixtures with TSRS polymer have lower average plane porosity ϕ and average fractal dimension D^b in the interlayer zone than that with DPCS polymer, except the mixtures with time interval of 20 s. For time interval of 20 s, the average plane porosity ϕ in the interlayer zone with TSRS polymer is higher 10.3 % than these with DPCS polymer. For time interval of 30 min, the average plane porosity ϕ and average fractal dimension D^b in the interlayer zone with TSRS polymer is lower 16.1 % and 1.5 % than these with DPCS polymer, respectively. For time interval of 60 min, the average plane porosity ϕ in the interlayer zone with TSRS polymer is lower 1.0 % than these with DPCS polymer.

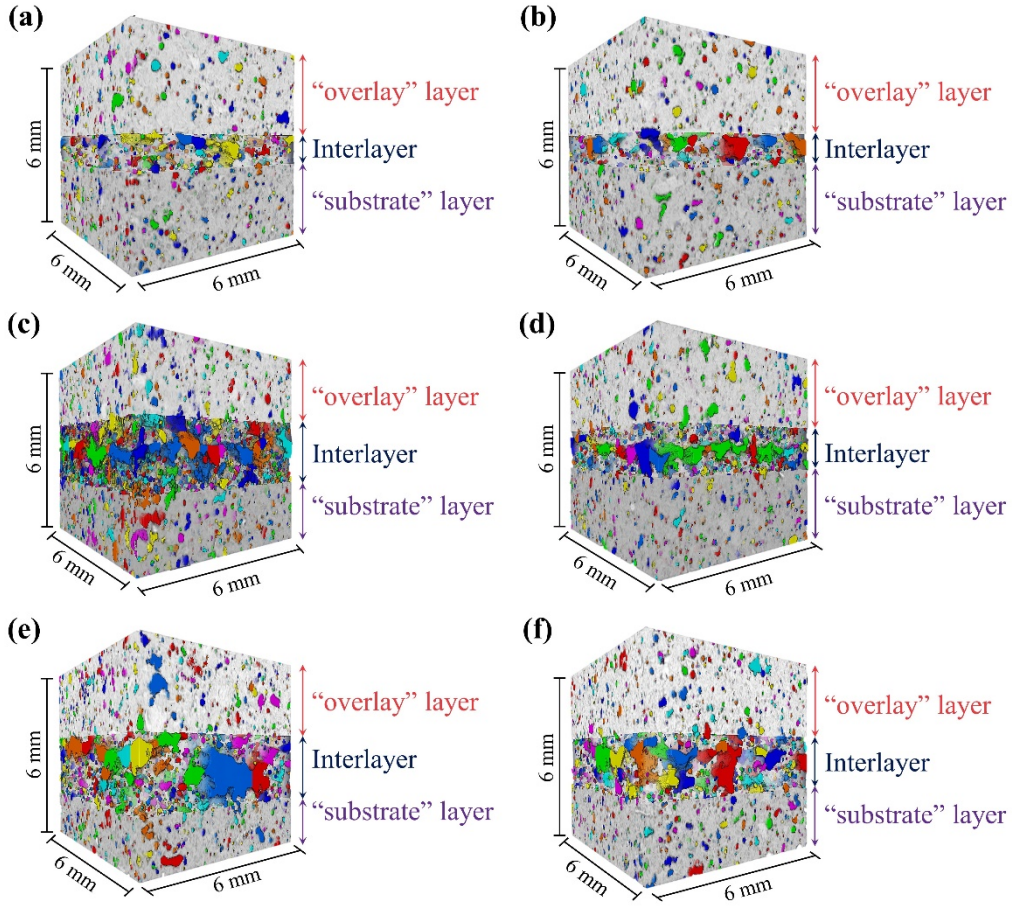


Fig. 10. Reconstructions of the 3D microstructure of 3D printed structures, which were obtained on the basis of tests using the micro-CT method for samples: (a) DPCS/T20, (b) TSRS/T20, (c) DPCS/T1800, (d) TSRS/T1800, (e) DPCS/T3600, (f) TSRS/T3600.

Fig. 10 shows the reconstruction of 3D microstructure of double-layer printed structures based on the CT slice image using X-CT test. Qualitative visual assessing these 3D models, it can be noted that there is a significantly interlayer zone between “substrate” layer and “overlay” layer, and the “substrate” layer, “overlay” layer and interlayer zone contains the microstructure with a significantly different size, number and space distribution of pores. Many unfilled areas and ‘wide’ macropores are concentrated on the interlayer zone of printed structures, which provides a channel for chloride or carbon dioxide ions ingress and is the possible reason for the weak interlayer bonding strength and bad durability properties of printed structures [15].

3.2.2 Maximum value of plane porosity and fractal dimension

The maximum value of plane porosity ϕ_{max} and fractal dimension D^b_{max} in the interlayer zone is therefore investigated and plotted in Fig. 11. Both of time interval and superplasticizer types significantly affect the maximum value of plane porosity ϕ_{max} and fractal dimension D^b_{max} in the interlayer zone.

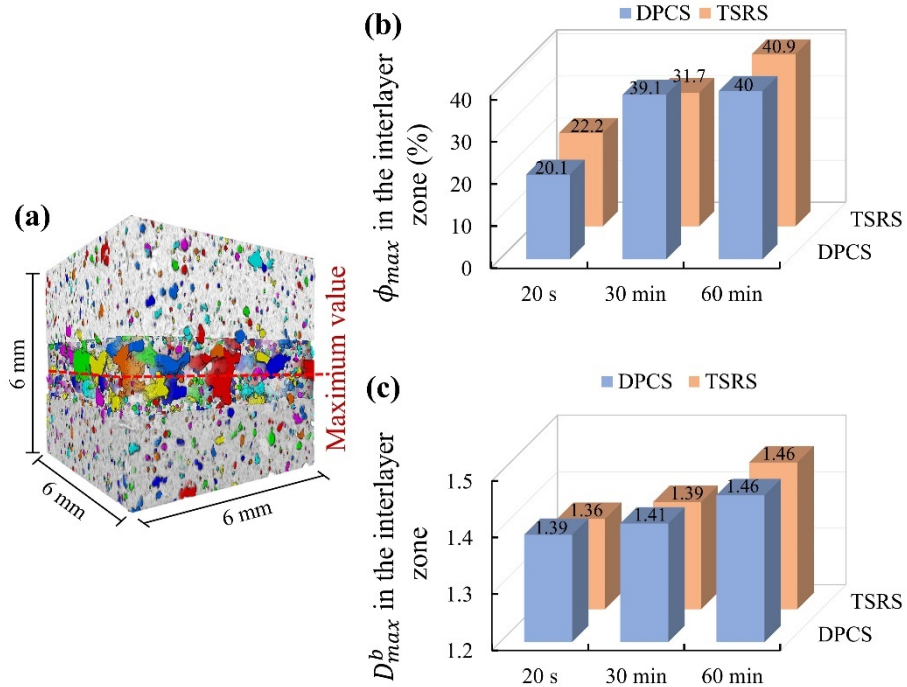


Fig. 11. Interlayer zone in the printed structures (a); The maximum value of plane porosity in the interlayer zone (b); The maximum value of fractal dimension in the interlayer zone (c).

As shown in Fig. 11(b, c), the value of ϕ_{max} in the interlayer zone increases with the extend of time interval, which is in good agreement with the results obtained by Yu et al. [51]. The values of ϕ_{max} and D^b_{max} in the interlayer zone with time interval of 20 s were lowest. Extending the time interval would result in a significant increase in these values. For the samples with DPCS polymer, the values of ϕ_{max} with time interval of 30 min and 60 min were higher 61.5 % and 71.5 % than that with time interval of 20 s, the values of D^b_{max} with time interval of 30 min and 60 min are higher 5.1 % and 9.4 % than that with time interval of 20 s, respectively. For the samples

with TSRS polymer, the values of ϕ_{max} with time interval of 30 min and 60 min were higher 50.2 % and 75.4 % than that with time interval of 20 s, the values of D^b_{max} with time interval of 30 min and 60 min are higher 5.9 % and 8.8 % than that with time interval of 20 s, respectively.

Furthermore, the printed structures with TSRS polymer always have lower values of ϕ_{max} and D^b_{max} than that with DPCS polymer. For time interval of 20 s, the values of ϕ_{max} and D^b_{max} with TSRS polymer are lower 11.6 % and 1.4 % than that with DPCS polymer. For time interval of 30 min, the values of ϕ_{max} and D^b_{max} with TSRS polymer are lower 17.8 % and 0.7 % than that with DPCS polymer. For time interval of 60 min, the values of ϕ_{max} and D^b_{max} with TSRS polymer are lower 9.6 % and 2.0 % than that with DPCS polymer.

3.3 Interlayer bond strength

Table 5 summarizes the interlayer bonding strength of 3D printed structures using uniaxial tensile test. Their statistical characteristics, such as mean value (\bar{f}_b) and standard deviation σ are also marked from three test results.

Table 5. The results of the interlayer bond strength f_b and their statistical characteristics.

Mixtures	No.	Interlayer bonding strength f_b (MPa)	Mean value \bar{f}_b (MPa)	Standard deviation σ (MPa)
DPCS/T20	1	1.97		
	2	1.85	1.86	0.11
	3	1.76		
	4	0.88		
DPCS/T1800	5	0.75	0.77	0.10
	6	0.68		
	7	0.48		
DPCS/T3600	8	0.39	0.39	0.09
	9	0.30		
	10	1.43		
TSRS/T20	11	1.75	1.74	0.30
	12	2.04		
TSRS/T1800	13	1.04		
	14	0.95	0.96	0.08

	15	0.89		
	16	0.30		
TSRS/T3600	17	0.41	0.40	0.04
	18	0.49		

From Table 5, the interlayer bond strength of printed structures with time interval of 20 s is biggest. They are 1.76 MPa and 1.94 MPa for the printed structures with DPCS polymer and TSRS polymer, respectively. Extending the time interval would significantly decrease the interlayer bond strength. For the printed structures with DPCS polymer, the interlayer bond strength of printed structures with time interval of 30 min and 60 min are lower 56.8 % and 77.8 % than that with time interval of 20 s, respectively. For the printed structures with TSRS polymer, the interlayer bond strength of printed structures with time interval of 30 min and 60 min are lower 50.5 % and 75.3 % than that with time interval of 20 s, respectively.

Furthermore, the printed structures with TSRS polymer always have higher interlayer bond strength than that with DPCS polymer. For time interval of 20 s, the interlayer bond strength of printed structure with TSRS polymer is higher 10.2 % than that with DPCS polymer. For time interval of 30 min, the interlayer bond strength of printed structure with TSRS polymer is higher 24.7 % than that with DPCS polymer. For time interval of 60 min, the interlayer bond strength of printed structure with TSRS polymer is higher 41.0 % than that with DPCS polymer.

3.4 Relationship between air–void systems and interlayer bonding strength

For a quasi–brittle 3D printed cement mortar, the interlayer bonding strength is closely related to the air–void systems within the interlayer zone [31, 51]. Fig. 12 shows the relations between the average plane porosity ϕ , average fractal dimension D^b , maximum plane porosity ϕ_{max} , maximum fractal dimension D_{max}^b and the interlayer bonding strength of 3D printed structures, respectively.

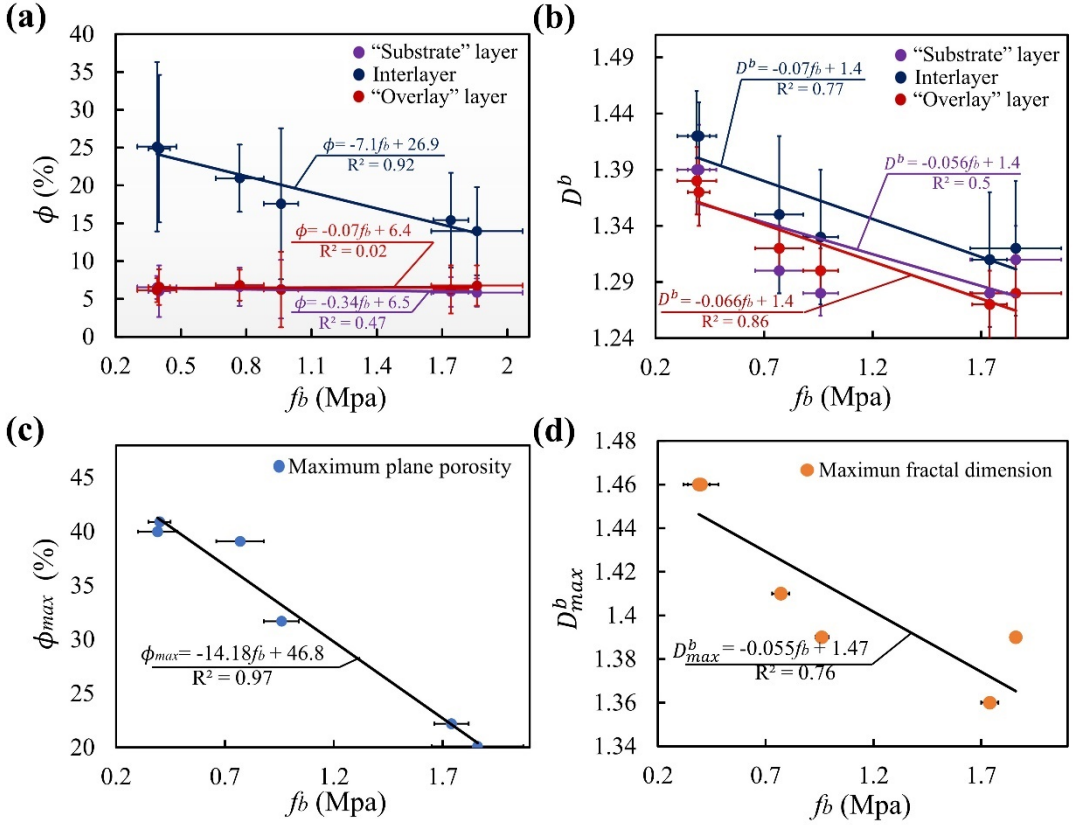


Fig. 12. The relations between the average plane porosity ϕ (a), average fractal dimension D^b (b), maximum plane porosity ϕ_{max} (c), maximum fractal dimension D^b_{max} (d) and the interlayer bonding strength of 3D printed structure.

As shown in Fig. 12, the value of ϕ_{max} and D^b_{max} are significantly related to the interlayer bonding strength, while the average plane porosity and average fractal dimension are weakly related to the interlayer bonding strength of 3D printed structures. Compared to the average value of plane porosity and fractal dimension, the maximum value of plane porosity and fractal dimension between the adjacent extruded layers seems to be a more critical factor to dominate the interlayer bonding strength, which is in good agreement with the results obtained by Lee et al. [52]. According to the principle of minimum energy consumption of fracture mechanics, the crack propagation path always follows the surface with the weakest bonding force [53]. Due to the weak adhesive of printed structures mainly concentrated on the interlayer zone, the microcracks propagates mainly along the interlayer zone in the tensile process, especially in the slice with the maximum plane porosity. Thus, the

value of ϕ_{max} and D^b_{max} of interlayer zone are significantly related to the interlayer bond strength. From Fig. 12, it can be found that the average plane porosity and average fractal dimension of “substrate” layer or “overlay” layer are not significantly related to the interlayer bond strength, indicating that the microcracks propagates mainly along the interlayer zone may suffer little influence by the microstructure of “substrate” layer or “overlay” layer.

4. Discussion

4.1 The effect of rheological properties on the interlayer bonding strength

In this paper, a high dispersion polycarboxylate superplasticizer (DPCS), and a slump-retaining polycarboxylate superplasticizer (TSRS) were selected to control the rheological properties of cement-based printing ink, of which the former obtains high initial fluidity and low initial static yield stress, and the latter has long duration of workability and plasticity.

For 3D printable cement mortars, long duration of fluid properties is expected not only an improvement in the extrudability or printability but also an increment in the maximum operational time (MOT) [34]. If the printing process is done off-site, long duration of fluid properties is recommended for successful printing, due to the sensitivity of rheology for printing [54]. Long duration of fluid properties is also critical for the printing process with long print paths. Furthermore, long duration of fluid properties is favorable for interlayer bonding of adjacent layers. As described by Courard et. al. [55], the contact between adjacent concrete may be attributed to the diffusion behaviour, penetration and capillary suction. Diffusion behaviour refers to the transfer of molecules or ions from high concentration region to low concentration region, which can be described by Fick's law [56]. Capillary suction is related to the transport of liquids into porous solids, due to interfacial tension between liquid and solid [33]. Penetration concerning the movement of liquids due to difference of pression [55]. In 3DPC, “overlay” layer may migrate downward induced by the gravity or external force to fill the pores and cracks on the surface of the “substrate” layer [57, 58], as shown in Fig. 13. Rheological property is one of the critical

parameters affecting the penetration behaviour between adjacent layers [58]. For TSRS polymer, the rate of structural build-up is slowed down and the fluidity (or workability) might last for a long time, it has a positive effect on the penetration of “overlay” layer to fill into the pores and cracks in the surface of “substrate” layer, thus resulting in an low porosity and high interlayer bond strength between the two zones, as reported in Fig. 8 and Table 5. Compared with TSRS polymer, DPCS polymer possess higher initial fluidity, which promotes the penetration and connect between adjacent layers with short time interval. This may be a possible reason for the higher interlayer bond strength and lower porosity of printed structures with time interval of 20 s. However, after a short period, the growth and nucleation of the hydration products entangling the hydrated cement particles suppresses its repulsive effect, which results in a large modulus/stiffness difference and limits the fusion between adjacent layers. This may explain why the interlayer bond strength of mixtures with DPCS polymer is lower than that with TSRS polymer at long time interval (30 min).

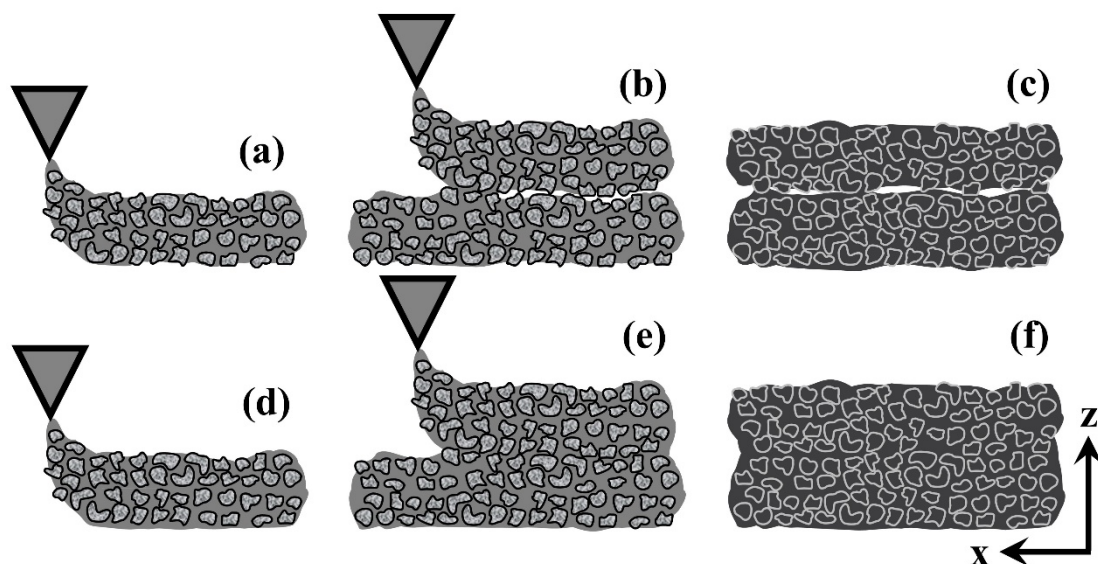


Fig. 13. Schematic diagram of spontaneous permeating of cement-based materials with complete layer bonding/filling of voids (a–c) and with incomplete layer bonding/filling of voids (d–f).

4.2 The effect of time interval on the interlayer bonding strength

For 3DPC, before the “overlay” layer is extruded, the previous deposited “substrate” layer had a certain degree of cement hydration [18]. The factor of time interval represents in fact the “pre-hydration” of “substrate” layer before the interface is generated. With the extending of time interval, hydration products such as ettringite and C–S–H forms bridges between binder grains thus the previous deposited “substrate” layer will gradually gain a certain strength [46]. If the “overlay” layer is printing during this period, it is difficult to excite surface activity of the “substrate” layer. Furthermore, insufficient hydration and high porosity is formed in the interfacial area, as reported in Fig. 10, due to the evaporation and drying of water on the surface of “substrate” layer [24, 59].

In addition, extending the time interval will increase the surface stiffness of the “substrate” layer [60], as shown in Fig. 14. Rough surface of “substrate” layer may result in more difficulty to the fusion between adjacent layers [61]. Extending the time interval also increase the relative shrinkage of “substrate” layer, which may result in shrinkage cracks at the interlayer zone and reduce the interlayer bond strength [27, 62].

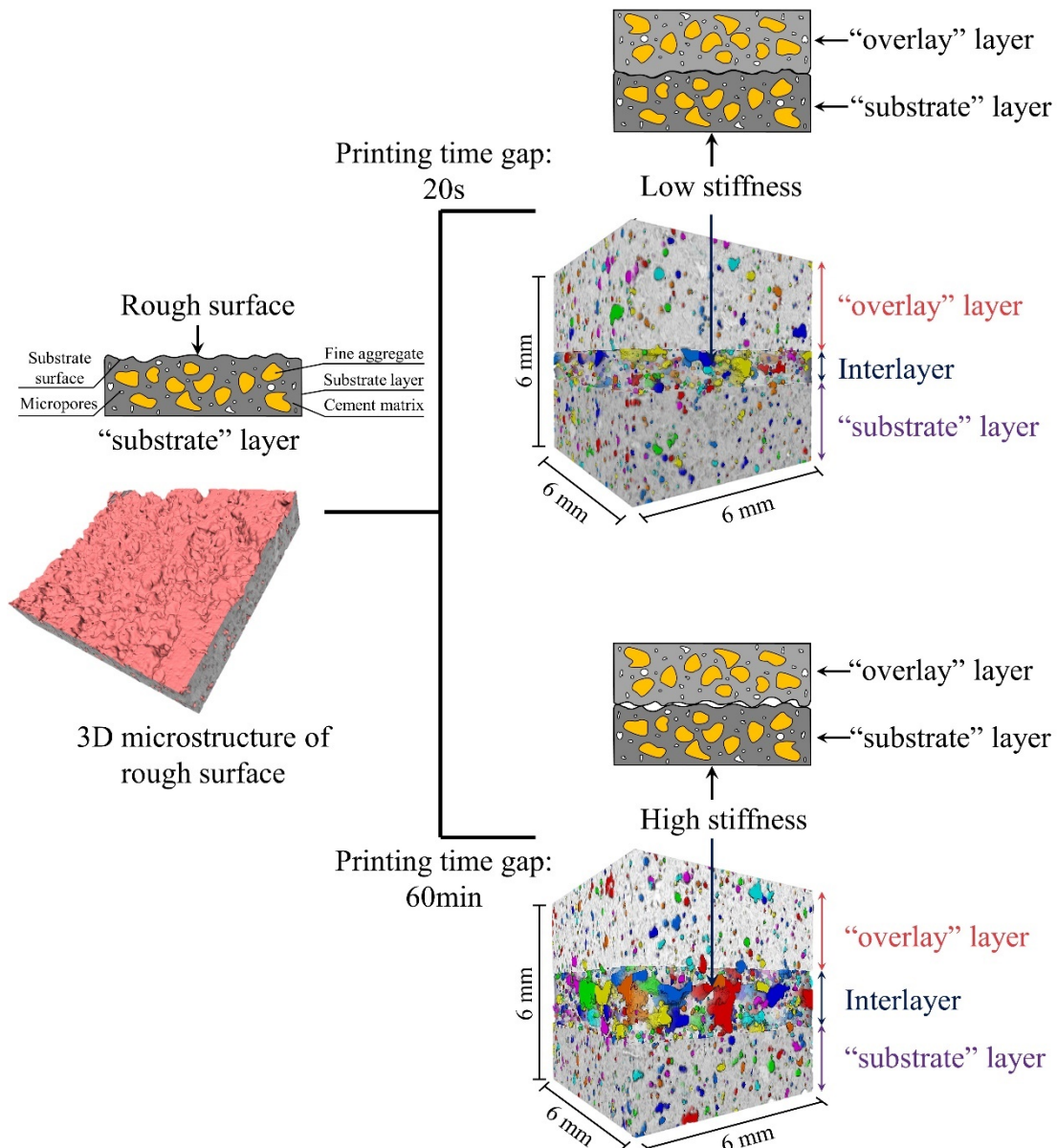


Fig. 14. Illustration of the influences of extending the time interval on air void formation at the interface.

5. Conclusions

In this paper, two different types of polycarboxylate superplasticizers (a high dispersion polycarboxylate superplasticizer DPCS and a slump-retaining polycarboxylate superplasticizer TSRS) were used to control the time-dependent rheological properties, and the physical and chemical state differences between adjacent layers were adjusted through different printing time intervals (20 s, 30 min

and 60 min). The rheological properties of 3D printable cement mortars with different types of polycarboxylate superplasticizer were characterized via BROOKFIELD RST-SST rheometer, the microstructure of 3D printed structure was measured by X-ray CT computed tomography system, and the interlayer bond strength of 3D printed structure was measured by direct tensile test. The following results are obtained:

- (1) Polycarboxylate superplasticizer can be used to adjust the rheological properties of fresh cement-based materials and its change law with time. The initial fluidity of slump-retaining polycarboxylate superplasticizer (TSRS) is slightly lower than that of high dispersion polycarboxylate superplasticizer (DPCS), while its loss of fluidity with time is lower than that of DPCS.
- (2) Excessive structural build-up rate results in a rapidly loss of workability and plasticity, which is recommended to ensure the buildability and stability of printed structures, but not conducive to the interlayer bonding of printed structures. The rapidly loss of workability of “overlay” layer will prevent its permeating to fill into the pores and cracks in the surface of “substrate” layer, and results in high plane porosity between adjacent print layers. Furthermore, the rapidly loss of workability of “substrate” layer will increase the surface stiffness difference between adjacent layers and decreases the interlayer bond strength of printed structures, especially for long time interval.
- (3) Long duration of fluid properties promotes permeate and fusion between adjacent printed layers, resulting in lower plane porosity and lower fractal dimensions of pore structures at the interlayer zone. 3DPC with less plane porosity and smaller fractal dimensions of pore structures at the interlayer zone has better interlayer bond strength.

Appendix A: Fourier transformer infrared spectra (FTIR) measure

The high dispersion polycarboxylate superplasticizer (DPCS), and the slump-retaining polycarboxylate superplasticizer (TSRS) were pressed disc with KBr to obtain FTIR data. The wavenumber in the range of 4000–400 cm⁻¹ are recorded on

Thermo Scientific Nicolet iS5.

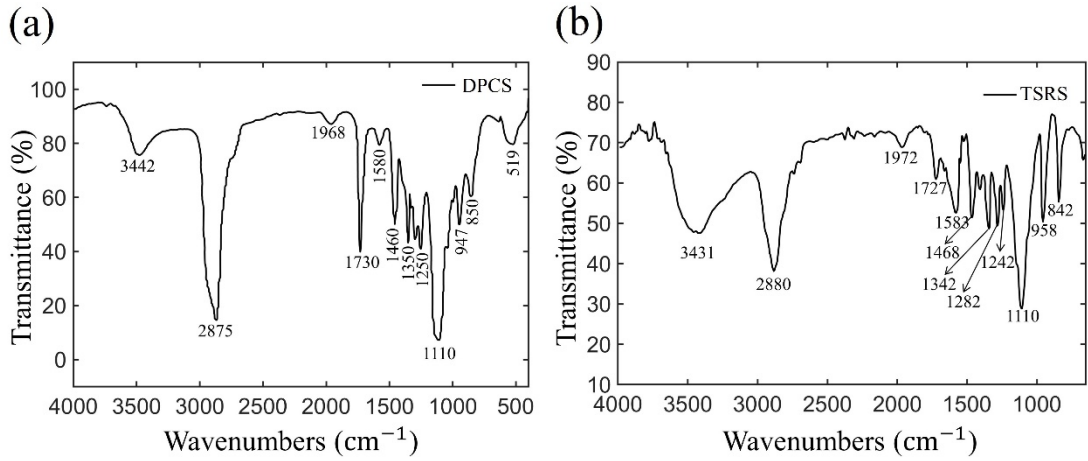


Fig. A1. FTIR spectra for DPCS and TSRS polymers.

FTIR spectra of DPCS and TSRS are reported in Fig. A1. The peak at about 3428 cm^{-1} is the stretching vibration peak of hydroxyl ($-\text{OH}$), the peak at about 2875 cm^{-1} is the characteristic vibrational absorption peak of C–H. The stretching vibration absorption peak of carboxyl at 1730 cm^{-1} , the peak at about 1460 cm^{-1} is corresponding to the C–H bending vibration absorption peak of methylene ($-\text{CH}_2-$), the peak at about 1345 cm^{-1} is corresponding to the $-\text{OH}$ bending vibration absorption peak of carboxyl, the peak at about 1110 cm^{-1} and 948 cm^{-1} are corresponding to the C–O–C bending vibration absorption peak, and the peak at about 845 cm^{-1} corresponding to the $-\text{CH}_2-$ bending vibration absorption peak. The FTIR results shows that the molecular structures of DPCS and TSRS polymers contain hydroxyl, carboxyl, ether, and other functional groups. In addition, from the FTIR spectra of TSRS, it can be found that there is a significant peak at about 1580 cm^{-1} , which may be the characteristic absorption peak of $-\text{NH}_2$, indicates that acrylamide is introduced into TSRS polymers. This may be a possible reason for the high slump retention of TSRS polymers.

Appendix B: Gel Permeation Chromatography (GPC) measure

The polymer molecules can be separated by the gel permeation chromatography

(GPC), due to their hydrodynamic volume of the polymer molecular is different. The molecular parameters of DPCS polymer and TSRS polymer are evaluated by weight-average molecular weight (M_w), the number-average molecular weight (M_n), the polydispersity index (PD: M_w/M_n). A gel permeation chromatograph (GPC) apparatus (PL-GPC50; PL-GPC220; Waters GPC 1515) is employed to determine M_w , M_n of SAF SP. In this work, 0.10 mol/L sodium nitrate solution (pH of the solution adjusted to 12 with NaOH) as carrying phase at a flow rate of 0.8 mL/min, the mono-dispersive sodium polyethylene sulfonate as the standard phase of calibration.

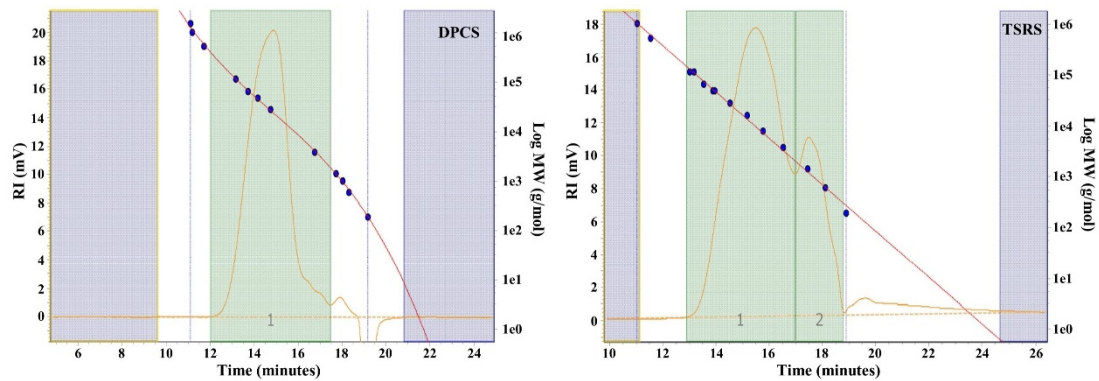


Fig. B1. The results of GPC.

Table B1. The molecular parameter of DPCS polymer and TSRS polymer.

Polymer	Peak Results	M_p (g/mol)	M_n (g/mol)	M_w (g/mol)	PD	Area (%)
DPCS	Peak 1	24532	19930	38993	1.956	100.00
TSRS	Peak 1	9764	7362	15373	2.088	76.02
	Peak 2	1198	860	1043	1.213	23.98

The molecular weight distribution is one of the most basic structural parameters of superplasticizers. For the polymers with lower molecular weight, it may obtain a shorter molecular chain, which may influence the slump-retention property; for the polymers with higher molecular weight, it may result in the bypass effect, influence the disperse effect of superplasticizers. The high dispersion polycarboxylate

superplasticizer (DPCS) and the slump-retaining polycarboxylate superplasticizer (TSRS) are analyzed by GPC, as shown in Fig. B1 and Table B1.

The weight-average molecular weight and number-average molecular weights of DPCS polymer are 38993 g/mol and 19930 g/mol, respectively. The weight-average molecular weight and number-average molecular weights of TSRS polymer are 15373 g/mol and 7362 g/mol in peak 1, respectively. GPC results shows that the monomer conversion rate of TSRS polymer is higher than that of DPCS polymer.

Appendix C: TOC adsorption measure

ET1020A Total organic Carbon (TOC) analyzer produced by Shanghai Euro Tech Ltd. is used to measure the adsorption amount of superplasticizer on the surface of cement particles. Two grams of PCs (DPCS polymer and TSRS polymer) with different concentrations (0.2, 0.4, 0.8, 1.2 and 1.6 g/L, respectively) are prepared. 5g cement powder is weighed and added into PCs solutions with different types and different concentration, respectively. All these mixtures are stirred with a glass rod for 5min, stood for 5min, centrifuged in a centrifuge for 20 min. The filtered solution was taken for total organic carbon analysis. The testing range is from 4 ppb to 4000 ppm. The adsorption capacity is tested at 10 min and 60 min respectively.

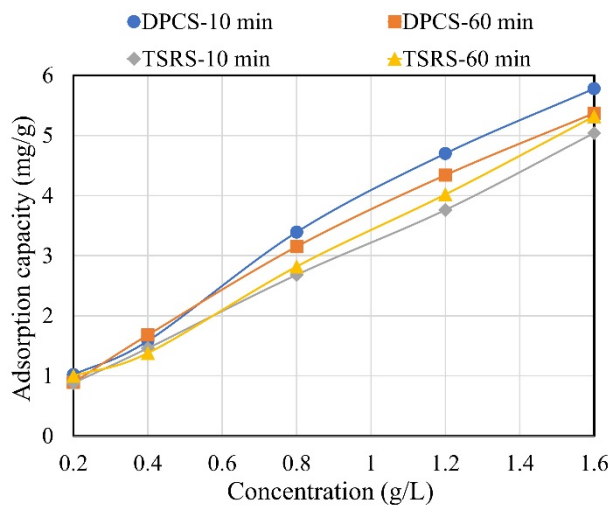


Fig. C1. The adsorption capacity of the DPCS polymer and TSRS polymer.

The adsorption capacity of the DPCS polymer and TSRS polymer at different concentrations on the surface of cement particles is studied. The adsorption curve is reported in Fig. C1. With the increases of the concentration of the superplasticizer, the adsorption capacity of cement particles to PCs is gradually increasing. The adsorption capacity of cement to the DPCS polymer is higher than that of TSRS polymer at 10 min, which may explain the higher flowability of cement mixture with DPCS polymer at the initial stage. Then, with the hydration of cement, the adsorption capacity of cement to the DPCS polymer at 60 min is lower than that at 10 min, while the adsorption capacity of cement to the TSRS polymer at 60 min is significantly higher than that at 10 min. This phenomenon may be explained by that with the cement hydration, the DPCS molecules adsorbed on the surface particles are continuously consumed, due to the deposition of hydration products on the surface of cement particles, which decreases the number of PCs molecules in solution and decreases the adsorption capacity of cement to the DPCS polymer. Conversely, with the hydration of cement, more TSRS molecules would be released into the solution due to the hydrolysis of acrylamide in alkaline environment, which increases the number of PCs molecules in solution and increases the adsorption capacity of cement to the TSRS polymer. This also explains why the fluidity–retention ability of the TSRS polymer is better than that of DPCS polymer.

CRediT authorship contribution statement

Yaqing Jiang: Conceptualization, Methodology, Investigation, Formal analysis, Writing – Original draft, Review and Editing. Tinghong Pan: Conceptualization, Methodology, Writing – Review and Editing, Supervision. Xuping Ji: Conceptualization, Methodology, Investigation, Formal analysis.

Declaration of competing interest

The authors declare that they have no known competing financial interests or personal relationships that could have appeared to influence the work reported in this paper.

Acknowledgments

This work was supported by the National Natural Science Foundation of China [grant numbers 51738003, 11772120].

References

- [1] J.G. Sanjayan and B. Nematollahi, 3D concrete printing for construction applications, *3D Concrete Printing Technology*, Elsevier (2019), pp. 1–11.
- [2] M.T. Souza, I.M. Ferreira, E.G. de Moraes, L. Senff and A.P.N. de Oliveira, 3D printed concrete for large-scale buildings: An overview of rheology, printing parameters, chemical admixtures, reinforcements, and economic and environmental prospects, *J. Build. Eng.* 32 (2020) 101833.
- [3] M.K. Mohan, A.V. Rahul, G. De Schutter and K. Van Tittelboom, Extrusion-based concrete 3D printing from a material perspective: A state-of-the-art review, *Cem. Concr. Compos.* 115 (2021) 103855.
- [4] A. Anton, L. Reiter, T. Wangler, V. Frangez, R.J. Flatt and B. Dillenburger, A 3D concrete printing prefabrication platform for bespoke columns, *Autom. Constr.* 122(2021) 103467.
- [5] C. Gosselin, R. Duballet, P. Roux, N. Gaudilli  re, J. Dirrenberger and P. Morel, Large-scale 3D printing of ultra-high performance concrete—a new processing route for architects and builders, *Mater. Des.* 100(2016) 102–109.
- [6] H. Alhumayani, M. Gomaa, V. Soebarto and W. Jabi, Environmental assessment of large-scale 3D printing in construction: A comparative study between cob and concrete, *J. Clean. Prod.* 270(2020) 122463.
- [7] D.H. Murcia, M. Genedy and M.R. Taha, Examining the significance of infill printing pattern on the anisotropy of 3D printed concrete, *Constr. Build. Mater.* 262(2020) 120559.
- [8] I. Agust  -Juan, F. M  ller, N. Hack, T. Wangler and G. Habert, Potential benefits of digital fabrication for complex structures: Environmental assessment of a robotically fabricated concrete wall, *J. Clean. Prod.* 154(2017) 330–340.
- [9] R.A. Buswell, W.L. De Silva, S.Z. Jones and J. Dirrenberger, 3D printing using concrete extrusion: A roadmap for research, *Cem. Concr. Res.* 112(2018) 37–49.

- [10] J. Xiao, G. Ji, Y. Zhang, G. Ma, V. Mechtcherine, J. Pan, L. Wang, T. Ding, Z. Duan and S. Du, Large-scale 3D printing concrete technology: Current status and future opportunities, *Cem. Concr. Compos.* 122(2021) 104115.
- [11] Y. Jacquet, A. Perrot and V. Picandet, Assessment of asymmetrical rheological behavior of cementitious material for 3D printing application, *Cem. Concr. Res.* 140(2021) 106305.
- [12] R. You, Effect of Early Strength, Retarding and Slump-retaining Components of Polycarboxylic Acid Admixture on Workability of Fresh Concrete, *IOP Conf. Ser. Mater. Sci. Eng.*, 631(2019) 22047.
- [13] Q. Yuan, Z. Li, D. Zhou, T. Huang, H. Huang, D. Jiao and C. Shi, A feasible method for measuring the buildability of fresh 3D printing mortar, *Constr. Build. Mater.* 227(2019) 116600.
- [14] C. Joh, J. Lee, J. Park and I. Yang, Buildability and Mechanical Properties of 3D Printed Concrete, *Materials.* 13(2020) 4919.
- [15] J. Kruger and G. van Zijl, A compendious review on lack-of-fusion in digital concrete fabrication, *Addit. Manuf.* 37(2021) 101654.
- [16] A.J. Babafemi, J.T. Kolawole, M.J. Miah, S.C. Paul and B. Panda, A Concise Review on Interlayer Bond Strength in 3D Concrete Printing, *Sustainability-Basel.* 13(2021) 7137.
- [17] J. Van Der Putten, G. De Schutter and K. Van Tittelboom, The effect of print parameters on the (micro) structure of 3D printed cementitious materials, T. Wangler (Ed.), RJ Flatteditors, Springer International Publishing, Cham (2019), pp. 234-244.
- [18] N. Roussel and F. Cussigh, Distinct-layer casting of SCC: The mechanical consequences of thixotropy, *Cem. Concr. Res.* 38(2008) 624–632.
- [19] K.P. Sooryanarayana, P. Stynoski and D. Lange, Effect of Vibration on the Rheology of Concrete for 3D Printing, *RILEM International Conference on Concrete and Digital Fabrication*, Springer, 2020, 353–359.
- [20] J.G. Sanjayan, R. Jayathilakage and P. Rajeev, Vibration induced active rheology control for 3D concrete printing, *Cem. Concr. Res.* 140(2021) 106293.

- [21] L. Jia, F. Zhao, K. Yao and H. Du, Bond performance of repair mortar made with magnesium phosphate cement and ferroaluminate cement, *Constr. Build. Mater.* 279(2021) 122398.
- [22] L. Courard, T. Piotrowski and A. Garbacz, Near-to-surface properties affecting bond strength in concrete repair, *Cem. Concr. Compos.* 46(2014) 73–80.
- [23] C. Hu and Z. Li, Property investigation of individual phases in cementitious composites containing silica fume and fly ash, *Cem. Concr. Compos.* 57(2015) 17–26.
- [24] T. Marchment, J. Sanjayan and M. Xia, Method of enhancing interlayer bond strength in construction scale 3D printing with mortar by effective bond area amplification, *Mater. Des.* 169(2019) 107684.
- [25] T.A. Soylev and R. François, Quality of steel-concrete interface and corrosion of reinforcing steel, *Cem. Concr. Res.* 33(2003) 1407–1415.
- [26] V.N. Nerella, S. Hempel and V. Mechtcherine, Effects of layer-interface properties on mechanical performance of concrete elements produced by extrusion-based 3D-printing, *Constr. Build. Mater.* 205(2019) 586–601.
- [27] G. Ma, N.M. Salman, L. Wang and F. Wang, A novel additive mortar leveraging internal curing for enhancing interlayer bonding of cementitious composite for 3D printing, *Constr. Build. Mater.* 244(2020) 118305.
- [28] N.M. Salman, G. Ma, N. Ijaz and L. Wang, Importance and potential of cellulosic materials and derivatives in extrusion-based 3D concrete printing (3DCP): Prospects and challenges, *Constr. Build. Mater.* 291(2021) 123281.
- [29] G. Ma, Y. Li, L. Wang, J. Zhang and Z. Li, Real-time quantification of fresh and hardened mechanical property for 3D printing material by intellectualization with piezoelectric transducers, *Constr. Build. Mater.* 241(2020) 117982.
- [30] B. Panda, N.A. Noor Mohamed, S.C. Paul, G. Bhagath Singh, M.J. Tan and B. Šavija, The effect of material fresh properties and process parameters on buildability and interlayer adhesion of 3D printed concrete, *Materials.* 12(2019) 2149.
- [31] D. Liu, B. Šavija, G.E. Smith, P.E. Flewitt, T. Lowe and E. Schlangen, Towards

understanding the influence of porosity on mechanical and fracture behaviour of quasi-brittle materials: experiments and modelling, *Int. J. Fracture.* 205(2017) 57–72.

- [32] Y.W.D. Tay, G.H.A. Ting, Y. Qian, B. Panda, L. He and M.J. Tan, Time gap effect on bond strength of 3D-printed concrete, *Virtual Phys. Prototyp.* 14(2019) 104–113.
- [33] L. Hanžič, L. Kosec and I. Anžel, Capillary absorption in concrete and the Lucas–Washburn equation, *Cem. Concr. Compos.* 32(2010) 84–91.
- [34] T. Pan, Y. Jiang, H. He, Y. Wang and K. Yin, Effect of Structural Build–Up on Interlayer Bond Strength of 3D Printed Cement Mortars, *Materials.* 14(2021) 236.
- [35] Y. Qian and G. De Schutter, Enhancing thixotropy of fresh cement pastes with nanoclay in presence of polycarboxylate ether superplasticizer (PCE), *Cem. Concr. Res.* 111(2018) 15–22.
- [36] S. Kawashima, M. Chaouche, D.J. Corr and S.P. Shah, Rate of thixotropic rebuilding of cement pastes modified with highly purified attapulgite clays, *Cem. Concr. Res.* 53(2013) 112–118.
- [37] Z. Zhao, M. Chen, J. Xu, L. Li, Y. Huang, L. Yang, P. Zhao and L. Lu, Mix design and rheological properties of magnesium potassium phosphate cement composites based on the 3D printing extrusion system, *Constr. Build. Mater.* 284(2021) 122797.
- [38] N. Roussel, Rheological requirements for printable concretes, *Cem. Concr. Res.* 112(2018) 76–85.
- [39] M. Chen, B. Liu, L. Li, L. Cao, Y. Huang, S. Wang, P. Zhao, L. Lu and X. Cheng, Rheological parameters, thixotropy and creep of 3D-printed calcium sulfoaluminate cement composites modified by bentonite, *Compos. Part B Eng.* 186(2020) 107821.
- [40] C. Dai, A. Wu, Y. Qi, Z. Chen and B. Li, Mechanical properties of paste slurry under constant shear rate in initial structure failure process, *Adv. Mater. Sci. Eng.* (2019) 2971563.
- [41] I. Ivanova and V. Mechtcherine, Effects of Volume Fraction and Surface Area of

Aggregates on the Static Yield Stress and Structural Build–Up of Fresh Concrete, Materials. 13(2020) 1551.

- [42] Q. Yuan, D. Zhou, K.H. Khayat, D. Feys and C. Shi, On the measurement of evolution of structural build–up of cement paste with time by static yield stress test vs. small amplitude oscillatory shear test, Cem. Concr. Res. 99(2017) 183–189.
- [43] H. Jiang, N. Jin, H. Ye, Y. Tian, X. Jin, Q. Zeng, D. Yan and X. Xu, Fractal characterization of non–uniform corrosion of steel bars in concrete beams after accelerated depassivation and seven–year natural corrosion, Materials. 12(2019) 3919.
- [44] B.B. Mandelbrot and B.B. Mandelbrot, The fractal geometry of nature, WH freeman New York 1982.
- [45] T. Ai, R. Zhang, H.W. Zhou and J.L. Pei, Box–counting methods to directly estimate the fractal dimension of a rock surface, Appl. Surf. Sci. 314(2014) 610–621.
- [46] N. Roussel, G. Ovarlez, S. Garrault and C. Brumaud, The origins of thixotropy of fresh cement pastes, Cem. Concr. Res. 42(2012) 148–157.
- [47] J. Kruger, S. Zeranka and G. van Zijl, An ab initio approach for thixotropy characterisation of (nanoparticle–infused) 3D printable concrete, Constr. Build. Mater. 224(2019) 372–386.
- [48] Y. Qian, K. Lesage, K. El Cheikh and G. De Schutter, Effect of polycarboxylate ether superplasticizer (PCE) on dynamic yield stress, thixotropy and flocculation state of fresh cement pastes in consideration of the Critical Micelle Concentration (CMC), Cem. Concr. Res. 107(2018) 75–84.
- [49] J. Plank and B. Sachsenhauser, Experimental determination of the effective anionic charge density of polycarboxylate superplasticizers in cement pore solution, Cem. Concr. Res. 39(2009) 1–5.
- [50] S. Jin, J. Zhang and S. Han, Fractal analysis of relation between strength and pore structure of hardened mortar, Constr. Build. Mater. 135(2017) 1–7.
- [51] Y. Chen, K. Jansen, H. Zhang, C.R. Rodriguez, Y. Gan, O. Çopuroğlu and E.

- Schlangen, Effect of printing parameters on interlayer bond strength of 3D printed limestone–calcined clay–based cementitious materials: An experimental and numerical study, *Constr. Build. Mater.* 262(2020) 120094.
- [52] H. Lee, J.J. Kim, J. Moon, W. Kim and E. Seo, Correlation between pore characteristics and tensile bond strength of additive manufactured mortar using X-ray computed tomography, *Constr. Build. Mater.* 226(2019) 712–720.
- [53] S. Khalilpour, E. BaniAsad and M. Dehestani, A review on concrete fracture energy and effective parameters, *Cem. Concr. Res.* 120(2019) 294–321.
- [54] M.T. Souza, I.M. Ferreira, E.G. de Moraes, L. Senff, S. Arcaro, J.R.C. Pessôa, M.J. Ribeiro and A.P.N. de Oliveira, Role of chemical admixtures on 3D printed Portland cement: Assessing rheology and buildability, *Constr. Build. Mater.* 314(2022) 125666.
- [55] L. Courard, A. Darimont, Appetency and adhesion: analysis of the kinetics of contact between concrete and repairing mortars, A. Katz, A. Bentur, M. Alexander, G. Arliguie (Eds.), Proceedings of the RILEM international conference, interfacial transition zone in cementitious composites, E&FN Spon, Haifa (1998), pp. 185–194.
- [56] A. Paul, T. Laurila, V. Vuorinen and S.V. Divinski, Fick’s laws of diffusion, In: Thermodynamics, Diffusion and the Kirkendall Effect in Solids; Springer International Publishing: Cham, Switzerland, 2014; pp. 115–139.
- [57] T. Sivarupan, N. Balasubramani, P. Saxena, D. Nagarajan, M. El Mansori, K. Salonitis, M. Jolly and M.S. Dargusch, A review on the progress and challenges of binder jet 3D printing of sand moulds for advanced casting, *Addit. Manuf.* 12(2021) 101889.
- [58] D. Weger, A. Pierre, A. Perrot, T. Kränkel, D. Lowke and C. Gehlen, Penetration of Cement Pastes into Particle–Beds: A Comparison of Penetration Models, *Materials.* 14(2021) 389.
- [59] B. Zareian and B. Khoshnevis, Effects of interlocking on interlayer adhesion and strength of structures in 3D printing of concrete, *Autom. Constr.* 83(2017) 212–221.

- [60] K.V. Subramaniam and X. Wang, An investigation of microstructure evolution in cement paste through setting using ultrasonic and rheological measurements, *Cem. Concr. Res.* 40(2010) 33–44.
- [61] Z. Geng, W. She, W. Zuo, K. Lyu, H. Pan, Y. Zhang and C. Miao, Layer-interface properties in 3D printed concrete: Dual hierarchical structure and micromechanical characterization, *Cem. Concr. Res.* 138(2020) 106220.
- [62] G.M. Moelich, J. Kruger and R. Combrinck, Plastic shrinkage cracking in 3D printed concrete, *Compos. Part B Eng.* 200(2020) 108313.